


Evolution of interphase stress over a crack propagation plane as a function of stress relief heat treatments in a PBF-LB/M AlSi10Mg alloy

Ilaria Roveda¹ | Tatiana Mishurova¹ | Alexander Evans¹ | Andrew N. Fitch² | Jan Haubrich³ | Guillermo Requena^{3,4} | Giovanni Bruno^{1,5} | Itziar Serrano-Munoz¹ 

¹Bundesanstalt für Materialforschung und -prüfung (BAM), Berlin, Germany

²European Synchrotron Radiation Facility, Grenoble Cedex 9, France

³Institute of Materials Research, German Aerospace Center (DLR), Cologne, Germany

⁴Metallic Structures and Materials Systems for Aerospace Engineering, RWTH Aachen University, Aachen, Germany

⁵Institute of Physics and Astronomy, University of Potsdam, Potsdam, Germany

Correspondence

Itziar Serrano-Munoz, Bundesanstalt für Materialforschung und -prüfung (BAM), Unter den Eichen 87, 12205 Berlin, Germany.
Email: itziar.serrano-munoz@bam.de

Funding information

Bundesanstalt für Materialforschung und -prüfung (BAM), Grant/Award Number: MIT1-2019-40; European Synchrotron Radiation Facility (ESRF), Grant/Award Number: MA-5011

Abstract

In this study, we compare the residual stress state in a laser powder bed fusion (PBF-LB/M) AlSi10Mg alloy in the as-built (AB) condition with that after two different heat treatments (265 °C for 1 h, HT1; and 300 °C for 2 h, HT2). The bulk residual stress (RS) is determined using synchrotron X-ray diffraction (SXR), and near-surface profiles are determined using laboratory energy-dispersive X-ray diffraction (EDXR). The EDXR results do not reveal any notable difference between the conditions at a depth of 350 µm, suggesting that the machining process yields a comparable residual stress state in the near-surface regions. On the other hand, the SXR results show that HT1 is more effective in relieving the bulk RS. It is observed that HT1 reduces the RS state in both the aluminium matrix and the silicon network. In addition, HT2 does not have a significant impact on relaxing the RS as-built state of the matrix, although it does induce a reduction in the RS magnitudes of the Si phase. It is concluded that the heat treatment stress relieving is effective as long as the Si-network is not disaggregated.

KEYWORDS

Interphase residual stress, Laboratory energy-dispersive X-ray diffraction (EDXR), PBF-LB/M AlSi10Mg alloy, Stress-relief heat-treatments, Synchrotron X-ray diffraction (SXR)

1 | INTRODUCTION

Additive manufacturing (AM) offers numerous advantages, including design freedom, reduced material waste, and the ability to fabricate complex geometries. Among the various materials used in AM, aluminium-silicon (Al-Si) alloys are highly appealing because of their favourable combination of processability, high specific strength and good thermal conductivity; at a relatively quite low material cost. During the AM Laser Powder Bed Fusion (PBF-LB/M) process, the irradiated material experiences large temperature fluctuations in a short time, leading to the build-up of thermal stress

This is an open access article under the terms of the [Creative Commons Attribution](https://creativecommons.org/licenses/by/4.0/) License, which permits use, distribution and reproduction in any medium, provided the original work is properly cited.

© 2024 The Authors. *Strain* published by John Wiley & Sons Ltd.

and the accumulation of residual stress (RS) after manufacturing.^{1,2} RS in structural components can considerably affect the fatigue behaviour. Therefore, RS in PBF-LB/M alloys needs to be reliably evaluated and controlled. Post-process heat treatments offer a corrective solution for tailoring the microstructure and relieve the (tensile) RS, with the ultimate goal of enhancing the material strength.³

PBF-LB/M Al-Si alloys are known to exhibit a disaggregation of the eutectic Si network and subsequent formation of spheroidal Si particles within the temperature range from 260 °C to 300 °C.⁴ The as-built (AB) PBF-LB/M AlSi10Mg microstructure is composed of micrometric α -aluminium grains, surrounded by an almost continuous eutectic silicon network. The increased strength of the AB material (as compared to the heat treated conditions) is due to the fact that the Si network is able to bear the main part of the external loading, as observed via in-situ synchrotron X-ray diffraction tensile tests.⁵ In addition, a fraction of the Si and Mg remains in the aluminium matrix, forming a supersaturated solid solution.⁶

After 1 h at 265 °C, the Si solute concentration significantly drops, whereas the eutectic network structure is still present.^{4,7} The Si atoms almost entirely precipitates from the supersaturated matrix. At 300 °C, the eutectic Si network disaggregates after sufficient ageing time, forming globularized Si particles. After 2 h at 300 °C, the mesostructure largely homogenizes, although the melting pool boundaries are still noticeable in certain regions.^{6,8}

While it is widely agreed that a T6 heat treatment (e.g., 520 °C/1h solutionizing and 160 °C/8h ageing) completely relieves macroscopic RS⁹ and improves mechanical performance,¹⁰ the impact of low-temperature heat treatments (i.e., <300 °C) remains mostly unexplored. Moreover, the T6 heat treatment can lead to some deleterious thermally induced porosity.^{11,12} Low-temperature heat treatments are able to relieve RS, while inducing reduced alterations to the original fine Si network; therefore preserving the high static strength characteristic of the as-built condition. Some results indicate a reduction in surface RS of 60-65% after a direct ageing at 170 °C for 6 h.¹³ It was also observed that stress relief heat treatments between 245 °C and 300 °C have a similar and significant effect on reducing and redistributing the surface residual stresses.^{14,15} However, published studies are limited to surface measurements: the bulk of the material is not yet investigated in detail. Furthermore, the residual stress state of silicon phase is barely examined.

Our previous study on the subject aimed at determining the changes in the bulk RS (by using neutron diffraction, ND) in the aluminium matrix after a heat treatment at 265 °C for 1 h.^{16,17} Nevertheless, the ND results exhibit a puzzling large scatter in the RS profiles, that was not observed when measuring at the subsurface via laboratory energy-dispersive X-ray diffraction (EDXRD). Hence, as continuation to the findings reported in,¹⁶ the present study aims to further determine whether low-temperature heat treatments (i. e., below the solutionizing temperatures and without ageing) are effective in relieving RS, both at the near-surface and in the bulk. Diffraction techniques are the most adapted tools since they are both phase specific and non-destructive. Specifically, the high-resolution synchrotron X-ray diffraction (SXR) method used in this investigation allows the detection of peaks belonging to the Si phase, thereby enabling a detailed investigation of the phase specific RS state. The ultimate goal is to provide a robust methodology to characterize the RS state within the plane where a fatigue crack will be subsequently propagated.

2 | MATERIALS AND METHODS

The investigated samples were produced at the German Aerospace Research Center (Deutsches Zentrum für Luft- und Raumfahrt e.V., DLR), Germany, using a Concept Laser M2 machine. The samples were built under argon atmosphere in the shapes of prisms (Figure 1a) using gas atomised AlSi10Mg powder with the following size distribution parameters: $d_{10} = 9.62 \mu\text{m}$, $d_{50} = 26.46 \mu\text{m}$, and $d_{90} = 47.34 \mu\text{m}$. The scan strategy consisted of 5 mm \times 5 mm squares manufactured using a 45° rotating square patterns of parallel scan vectors, as shown in Figure 1b. The longest edge of the sample (height, 112 mm) was parallel to the building direction (BD). A laser power of 380 W with a scanning speed of 1500 mm/s was adopted. The layers had a 30 μm thickness and the hatching distance was 100 μm . The outer contours were scanned after processing the bulk material, using a standard contour strategy consisting of a single scan with a laser power of 180 W and scanning velocity of 1600 mm/s. The samples were built on a preheated platform kept at 200 °C during the entire process.

Two prisms were subjected to heat treatments, at 265 °C for 1 h (HT1) and at 300 °C for 2 h (HT2) performed using a PEO-630 furnace and followed by air cooling with a cooling rate of 10 °C/min. The 265 °C/1 h heat treatment is chosen because is considered the highest temperature to be reached before the silicon network starts disaggregation and subsequent formation of spheroidal Si particles.⁴ The 300 °C/2 h heat treatment is considered standard practice in Al-Si alloys to relieve RS.

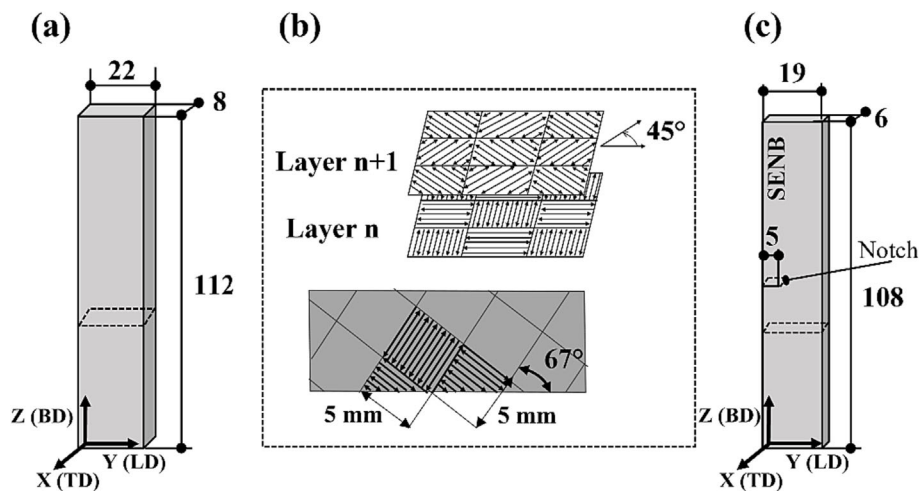


FIGURE 1 Samples production and manufacturing: schematic illustration of (a) the initial geometry, (b) the scanning strategy, and (c) the final single edge notch bending (SENB) geometry.

To avoid any distortion, the samples were machined to the final Single Edge Notched Beam (SENB) shape shown in Figure 1c after HT. More in detail, the surface finishing process involved an initial milling, where approximately one millimetre of material was removed from each side of the specimen. Following this, a grinding procedure was employed to achieve the final dimensions, resulting in a surface finish characterized by a roughness average (R_a) of 0.8. The selection of the Single Edge Notched Beam (SENB) geometry for our investigation was driven by the aim to subsequently investigate the fatigue propagation behaviour of the material. The SENB configuration is a widely recognized and standardized geometry, which is extensively used in fatigue studies, primarily due to its ability to induce controlled stress conditions, notably stress concentrations at the notch tip.¹⁸

Figure 2a-c present secondary electrons (SE) scanning electron microscope (SEM) micrographs (obtained using a LEO 1530VP field emission scanning electron microscope) of the microstructural changes induced by the post-process heat treatments. An electron backscatter diffraction (EBSD, using a Bruker Nano e-Flash detector) orientation map of the grain structure is shown in Figure 2d. The EBSD acquisition parameters are as follow: 0.6 μm step size, 20 keV acceleration voltage, 7–8 nA probe current, and 16 mm working distance.

As expected, HT1 induced the coarsening of the eutectic Si network, whereas HT2 led to the disaggregation of the Si phase into individual isolated particles (Figure 2a–c). In addition, the inverse poles figures show that the material possesses a [001] // BD texture with a maximum multiples of unity distribution (MUD) of 4.1 (Figure 2e). This type of texture is also widely documented in the literature (see for e.g.,¹⁹). For a more detailed description of these microstructures, the reader is referred to our previous publications on the subject.^{16,18}

The RS state was investigated via laboratory energy-dispersive X-ray (EDXRD) and Synchrotron X-ray diffraction (SXRD). High-energy Synchrotron X-rays are used for the investigation of the specimen bulk, because of their high penetration into matter. SXRD was performed at the high-resolution powder diffraction beamline ID22, at the European Synchrotron Radiation Facility (ESRF), France.^{20–22} A schematic of the set-up is shown in Figure 3a. A monochromatic X-ray beam of 60 keV energy was used in transmission mode; a single-channel analyser crystal detector set-up was employed. Adopting a wavelength of about $\lambda = 0.207 \text{ \AA}$, the 311 Si peak (at $\approx 2\theta = 7.2^\circ$) was chosen, in addition to the Al 311 diffraction peak (located at $\approx 2\theta = 9.7^\circ$). These Al 311 and Si 311 diffraction peaks were selected for stress calculation because they are reported to exhibit the lowest intergranular strains.²³

In SXRD at high energies (i.e., 60 keV), the diffraction angles are usually low, for example, the Al 311 reflection occurs at $2\theta \approx 10^\circ$. Therefore, it was not possible to measure the transversal direction (TD), since the beam would need to be transmitted through a thickness of 19 mm. We, nevertheless, assumed plane stress ($\sigma_{TD} = 0$) to calculate the stresses from the measured strains. The plane stress assumption was based on a previous triaxial RS evaluation by the authors using neutron diffraction (ND), where the very same samples at the same regions of interest were also analysed.¹⁶

The SXRD measurements were performed in the building and longitudinal directions (BD, LD) along a line (v) in the centre the notch plane and on two lines at 1.5 mm from the lateral surfaces: (vi) and (vii), as shown in the centre of Figure 3b. On the other hand, the EDXRD measurements were performed at the lateral surfaces at 27 mm distance

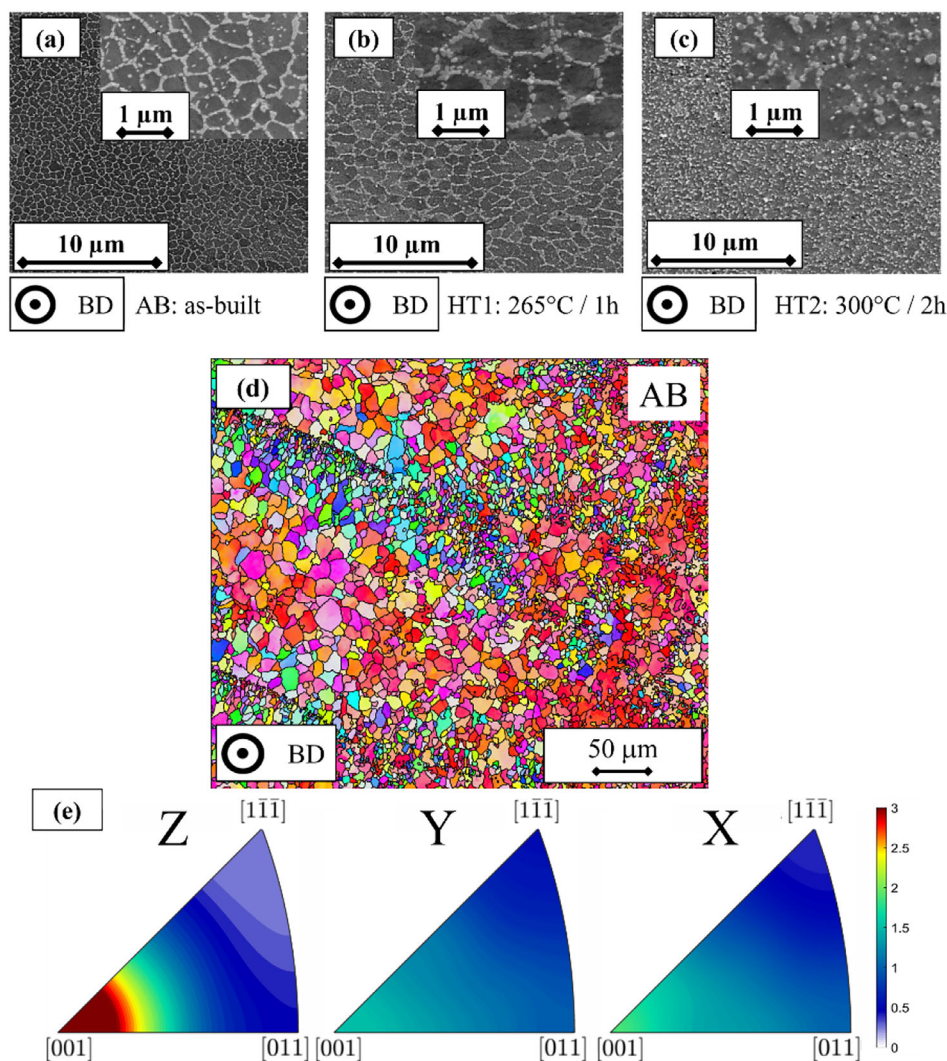


FIGURE 2 SEM-SE representative micrographs at different magnifications in the cross-section for the (a) as-built (AB), (b) after 1 h at 265°C (HT1), and (c) after 2 h at 300°C (HT2) conditions. (d) EBSD orientation map with respect to the building direction in the as-built condition, with (e) the respective Z (BD), Y (LD), and X (TD) inverse pole figures. This figure is readapted from.^{16,18} Note that the two curvature lines show in (d) correspond to melt pool boundaries.

from the notch plane along the height (named as nominal plane, Figure 3b, left side), as well as over a 2 mm by 4 mm region adjacent to the notch (Figure 3, right side).

The sample orientations adopted for the measurements and the dimensions of the gauge volume are schematised in Figure 4. A 0.225 mm × 2 mm beam was used, leading to a gauge length of 2.87 mm (through the specimen thickness). The measurement time per point was approximately 3 min. The specimen orientation was consequently changed to align the scattering vector to the geometric axis: vertical position in order to measure the BD component (Figure 4a, c), and horizontal position to measure the LD component (Figure 4b, d). It must be noted that while performing SXRD and EDXRD, it is assumed that there are no strong strain gradients occurring at the locations of the measuring points, either at the bulk along lines iv-vi, or at the subsurface along lines i-iii.

To compute strains and then stress from diffraction experiments, it is necessary to determine a stress-free reference. For this purpose, a 2 mm thick slice was extracted from the central part of a sister as-built prism (see Figure 5a). Subsequently, small, interconnected coupons measuring 2 mm × 2 mm × 2 mm were produced from this slice using electrical discharge machining (EDM). The coupon cutting followed a specific pattern indicated by the black solid lines shown in Figure 5b. This process aimed for the relaxation of macroscopic RS.

The grid was further cut down into three parts (indicated by the red dashed lines, Figure 5b), in order to investigate the d_0 variation after heat treatments. SXRD was performed on three coupons for each condition, in the TD and LD,

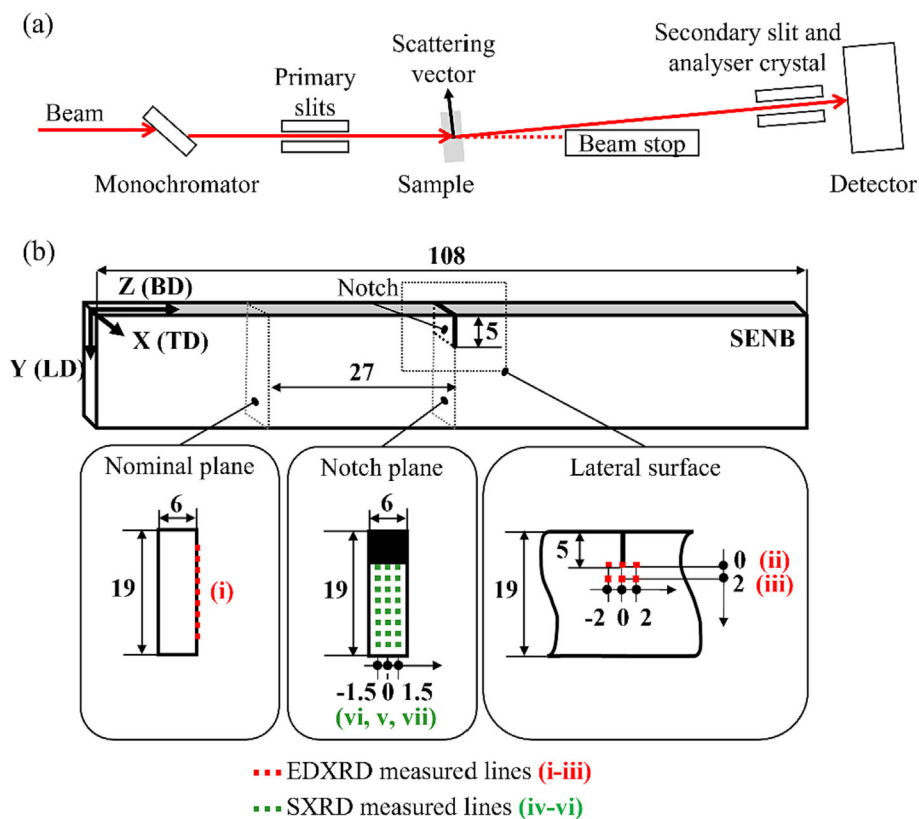


FIGURE 3 (a) Schematics of the ESRF-ID22 beamline set-up for SXR,²⁰ and (b) measured points in the SENB specimen: near-surface RS are measured by EDXRD on lines (i-iii) and bulk RS are measured by SXR on lines (iv-vi).

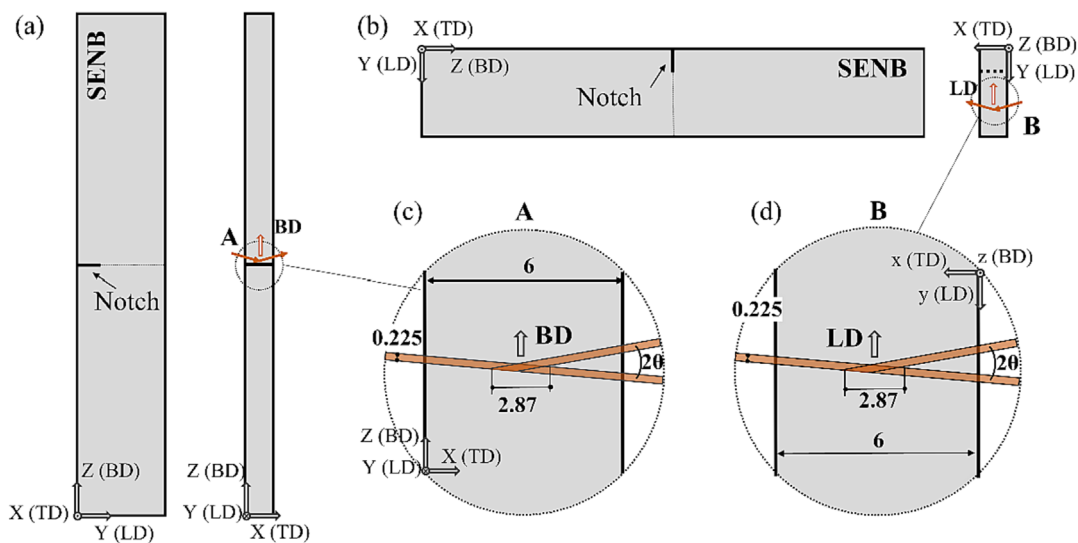


FIGURE 4 Schematics of the configurations adopted for the SXR measurements on the SENB specimens for the (a) BD and (b) LD directions. The gauge length through the thickness is described more in detail for the (c) BD measurements and (d) LD measurements. Note that the sample was tilted by using a rotation around X (TD) axis with an angle equivalent to θ to ensure that the scattering vector was aligned to the main geometrical axes.

using a beam size of $1 \text{ mm} \times 1 \text{ mm}$, to maximise the volume averaged (and increase the diffraction signal). The average of all six measured values per condition was adopted as stress-free reference. It was observed, in our previous study using neutron diffraction,¹⁶ that the d_0 -spacing reference varies as a function of the direction: the average d_0 in the BD

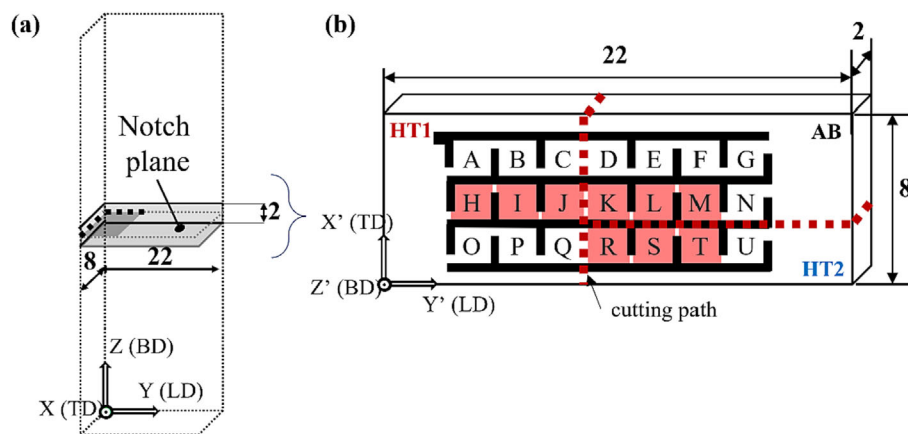


FIGURE 5 Schematic of the grid of interconnected coupons for the determination of the stress-free reference d_0 : (a) location of the extracted material in a sister specimen, (b) grid geometry (in thick black lines) and the cutting path, indicated with red dashed lines, used to divide the slice into three parts (needed to apply different heat treatments). The coupons measured during SXRD experiments are shown in red.

direction yields slightly higher values when compared with the LD and TD directions. Since this difference is small (0.05%), it is considered that the fact of using the LD+TD d_0 average has a marginal effect on the calculated stresses. This BD to LD-TD anisotropy has also been reported to occur in other PBF-L/M materials such as IN718 and 316L.^{24–26}

Regarding the silicon phase, a d_0 reference for was obtained by deep etching the Al phase using an 80% HCl + 20% H₂O solution. This treatment allows the removal of all the interphase stresses resulting from the interaction between the silicon and aluminium phases. The Si deposits (powder) were measured in glass capillaries with a diameter of 1 mm, using the same 1 mm × 1 mm beam size as that used for the coupons. The measurement was repeated three times for each heat treatment condition (AB, HT1 and HT2) and the average values for each condition were adopted as Si d_0 reference. The procedure followed for the calculation of RS is described in the Supplementary [Material](#).

The subsurface RS state was determined by energy-dispersive X-ray diffraction (EDXRD) carried out at the X-ray Corelab, Helmholtz-Zentrum Berlin für Materialien und Energie (HZB), Berlin.²⁷ The X-ray Corelab laboratory is equipped with a liquid-metal-jet X-ray source, providing higher brightness and spot sizes than other available laboratory microfocus X-ray sources. Therefore, it allows a greater penetration depth: up to 500 μm in a lightweight aluminium alloy can be penetrated using reflection geometry. We determined the RS using the Al 311 diffraction peak. The measurements were performed with a 1 mm pinhole polycapillary and a constant diffraction angle of $2\theta = 16.6^\circ$; this set-up allows a penetration depth of about 350 μm for the Al 311 peak. The RS were determined using the $\sin^2\psi$ method, assuming a nearly biaxial stress condition (i.e., assuming the stress component normal to the free surface to be negligible). The $\sin^2\psi$ method offers the advantage of not requiring a stress-free reference for strain calculations but can be used only in reflection geometry with the assumption of plane stress. The measurement time per point was 5 min.

Finally, the defect distribution in the prisms was investigated by means of X-ray computed tomography (XCT). We used an in-house assembled tomograph at the Bundesanstalt für Materialforschung und -prüfung (BAM, Berlin, Germany) featuring a Microfocus X-ray tube XWT-225-SE from X-Ray WorX GmbH (Garbsen, Germany) and a XRD1620 detector from PerkinElmer Inc. (Waltham, MA, USA). Further details on the tomograph set-up and data processing procedure can be found in.^{16,17}

3 | RESULTS

As shown in Figure 5, the stress-free reference variation as a function of the condition was measured using nine coupons of the grid, namely H-I-J, for the AB condition, K-L-M, for HT1 and R-S-T, for HT2. The plot shown in Figure 6 shows the spatial variation in the cross-section of the TD component. The d -spacing values are broadly uniform in the region of the grid subjected to the same heat treatment. The heat treatments have a homogenization effect, while the

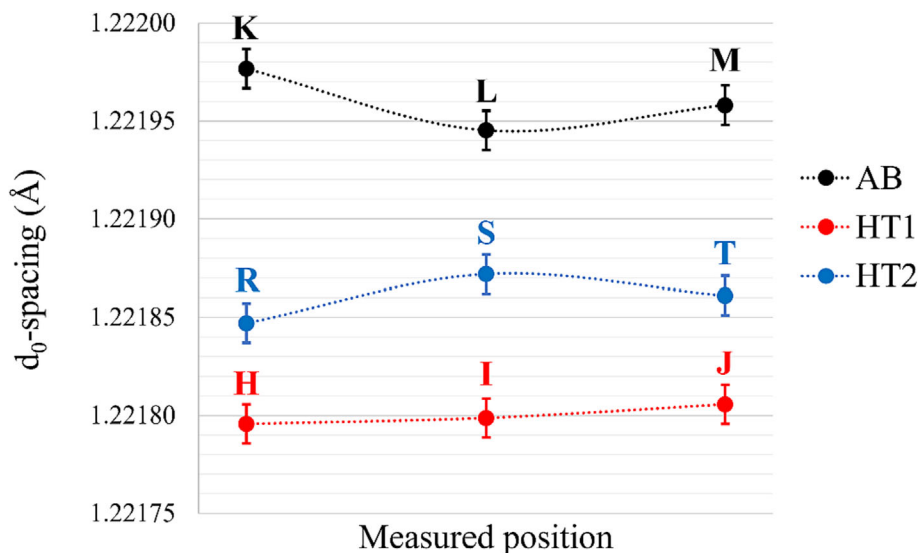


FIGURE 6 Average (using the LD and TD directions) of the d_0 -spacing values measured via SXRD. The coupons are in different states: coupons K-L-M correspond to the AB condition, H-I-J to HT1, and R-S-T to HT2.

TABLE 1 Results of the stress-free reference d_0 measured with SXRD for the AB, HT1 and HT2 conditions.

d_0-spacing (Å)		
Diffraction peak Method	Al {311} Coupons (average)	Si {311} Powder/Residue (average)
AB	1.22196 ± 0.00001	1.6417 ± 0.0001
HT1	1.22180 ± 0.00001	1.63894 ± 0.00008
HT2	1.22186 ± 0.00001	1.6383 ± 0.0001

AB condition exhibits a slightly increased spatial variation, most certainly resulting from local inhomogeneities of the cooling rates during the processing.

The averages of d_0 reported in Table 1 show that HT1 and HT2 result in similar values, while AB has slightly different d_0 . The values of d_0 for the Si phase, obtained by powder diffraction, are also reported in Table 1 for the different conditions. Again, no significant variation is observed between the two heat-treated conditions.

The stress profiles of the Al and Si phases in the SENB specimen notch plane (line (v) in Figure 3) are presented for the AB, HT1, and HT2 conditions in Figure 7. Similar trends are observed for lines (vi) and (vii) located at 1.5 mm depth from the surface, and the corresponding results are provided in the Supplementary material.

Moving away from the notch-affected region ($Y > 8$ mm), the stress profiles flatten. In the BD, the average stress value for the AB condition is about 50 MPa, which decreases to about 20 MPa after HT1 and to 40 MPa after HT2. The RS profiles of the silicon phase show a similar trend but with negative sign: away from the notch and the free surface, where the stress tends to zero, the stress profiles exhibit a flat behaviour. The average stress value for the BD is about -500 MPa in the AB condition, it reduces to about -250 MPa after HT1 and to -320 MPa after HT2. A similar evolution is observed for the LD, with relatively lower tensile stress values for the aluminium matrix and compressive values for the silicon phase. Interestingly, the average magnitudes are higher for HT2 when compared with HT1. The sharp deviations observed in the AB specimen at $Y = 10$ mm and $Y = 11$ mm has a large measurement error (Figure 7c). These deviations are thought to be caused by a significant local increase of gas porosity clustering.

The subsurface RS determined in the aluminium matrix in the AB condition and after heat treatments on the lines (i-iii) shown in Figure 3 are compared in Figure 8. Since similar values are obtained after measuring both the front and back surfaces of the specimen, only the RS profiles from the front side are presented. The near-surface region exhibits similar magnitudes of compression in all the conditions, with an average value of ≈ -70 MPa in the BD and ≈ -80 MPa

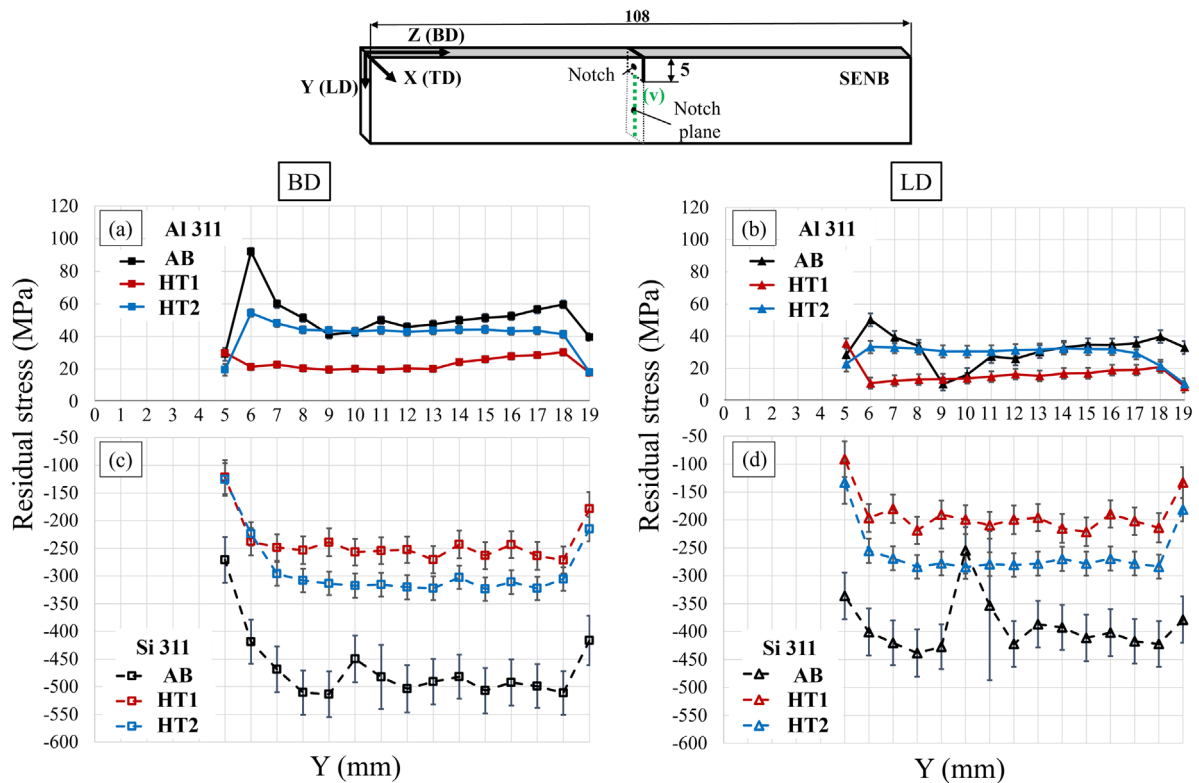


FIGURE 7 Bulk RS profiles before and after heat treatments over the notch plane for the (a, c) BD and (b, d) LD components. The results correspond to the Al 311 (a, b) and the Si 311 (c, d) peaks of the AB (black), HT1 (red) and HT2 (blue) conditions. The average error associated is ± 5 MPa for the Al and ± 40 MPa for the Si.

in the LD. Moreover, a fluctuating trend is observed in the profiles. The fluctuations are most probably due to the influence of aligned porosity clusters, as occurs in the ND measurements.¹⁶

A summary of the RS state in the aluminium matrix for the BD, which would correspond to the loading direction during fatigue crack propagation testing, is shown in the contour plots of Figure 9, using a linear interpolation. The graph combines the near-surface measurements obtained via laboratory EDXRD (lines at $X = 0$ and 6 mm) with the SXRD bulk measurements (lines at $X = 1.5, 3$ and 4.5 mm). The RS in the Al phase determined on the crack propagation plane before testing is compressive at the surface and tensile in the bulk in all the investigated conditions. The RS at the notch tip, where the crack would initiate during fatigue crack propagation tests, is tensile for all the conditions, with the highest magnitudes corresponding to the AB condition and the lowest to the HT1 sample.

4 | DISCUSSION

4.1 | On the evolution of interphase stress

The results obtained by SXRD measurements reveal that modifications in the morphology of the Si phase have a direct impact on the bulk RS state. Regarding the d_0 values, it is observed that both heat-treatments have a homogenising effect on the chemistry.

To appreciate better the effect of the heat treatments, the RS ranges, namely the difference between maximum and minimum values of the profiles in Figure 7, are shown in the bar charts of Figure 10. The heat treatment at 265 °C (HT1), which mostly involves the rejection of silicon from the supersaturated aluminium matrix, leads to a stress relaxation in both the aluminium matrix (approximately 60%) and the eutectic silicon network (approximately 50%). In the HT1 condition, as well as in the AB, we have the configuration where a soft Al matrix is enclosed by cells, where the walls contain a harder Si phase.

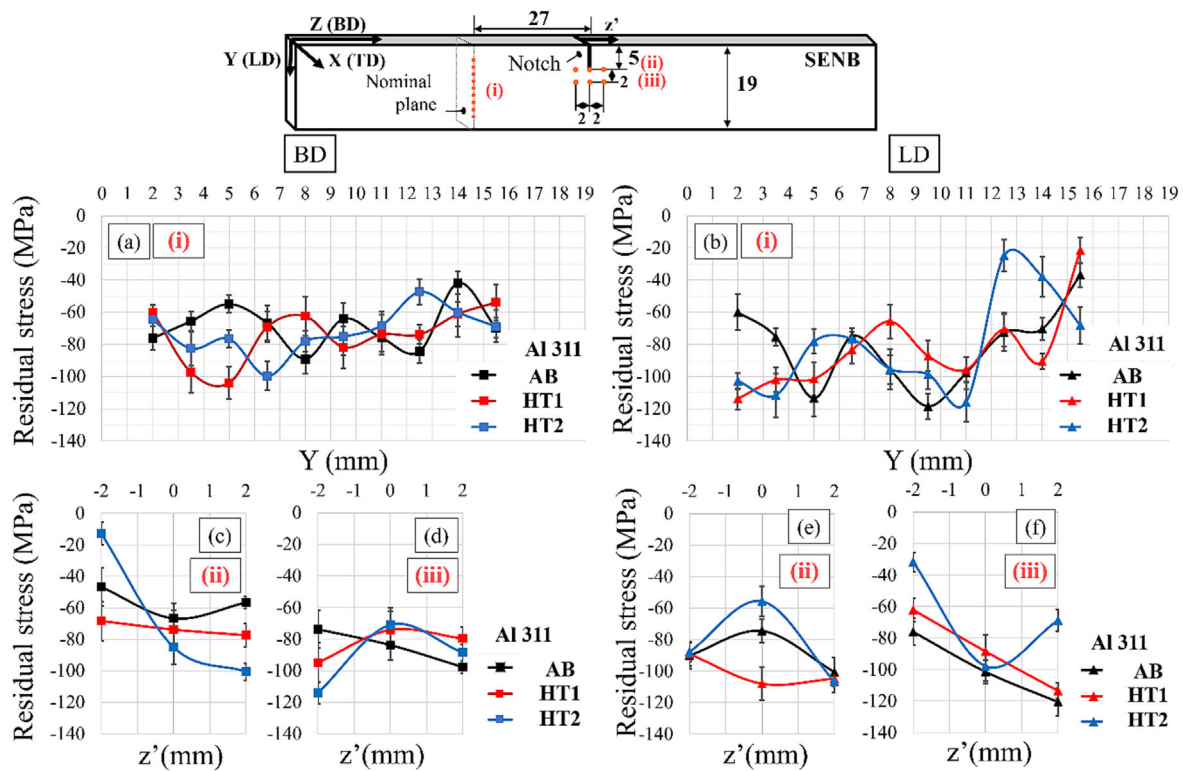


FIGURE 8 Near-surface RS before (AB, black) and after heat treatments (HT1, red and HT2, blue) at the BD (a, c, d) and LD (b, e, f) axes. Profiles measured (a, b) along a line (i) at 27 mm from the notch plane and (c–f) on some points ahead of the notch tip (lines (ii) and (iii)). The average error associated is ± 10 MPa.

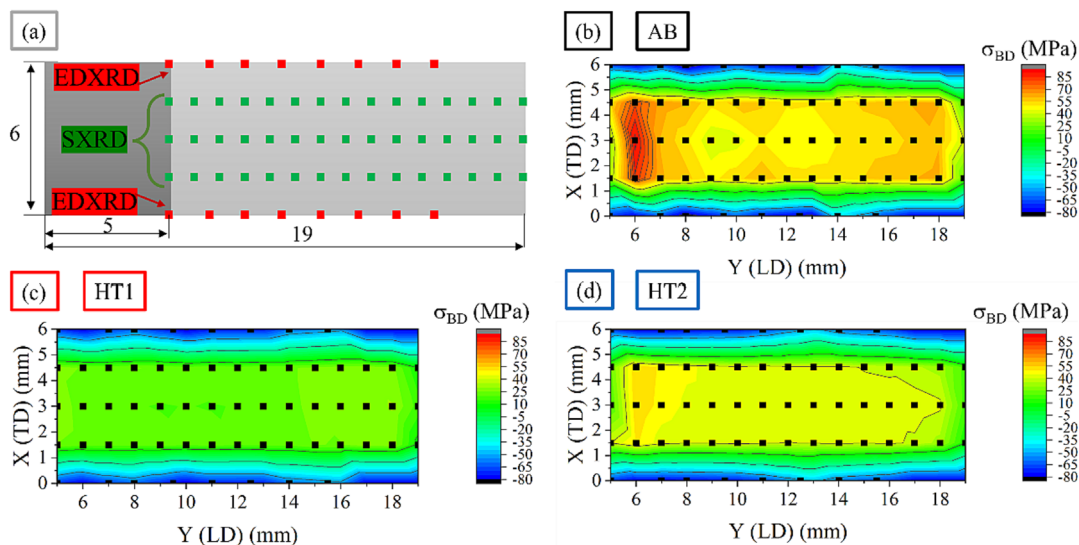


FIGURE 9 Linear contour plots of the Al-phase residual stress state on the crack plane in the loading direction (BD) before testing. As shown by the scheme in (a), the plots summarise the results from synchrotron and laboratory X-ray diffraction for the three studied conditions: (b) AB, (c) HT1 and (d) HT2.

HT2 leads to the disaggregation and spheroidization of the Si phase, which recombines the Si network into a composite formed by hard particles embedded in a soft matrix. This recombination leads to higher compression magnitudes in the silicon particles, as well as higher tension magnitudes in the aluminium matrix, when compared to HT1. Given that the crystal lattice structure of Si phase is 21% larger than that of FCC Al matrix, one would expect the increase in

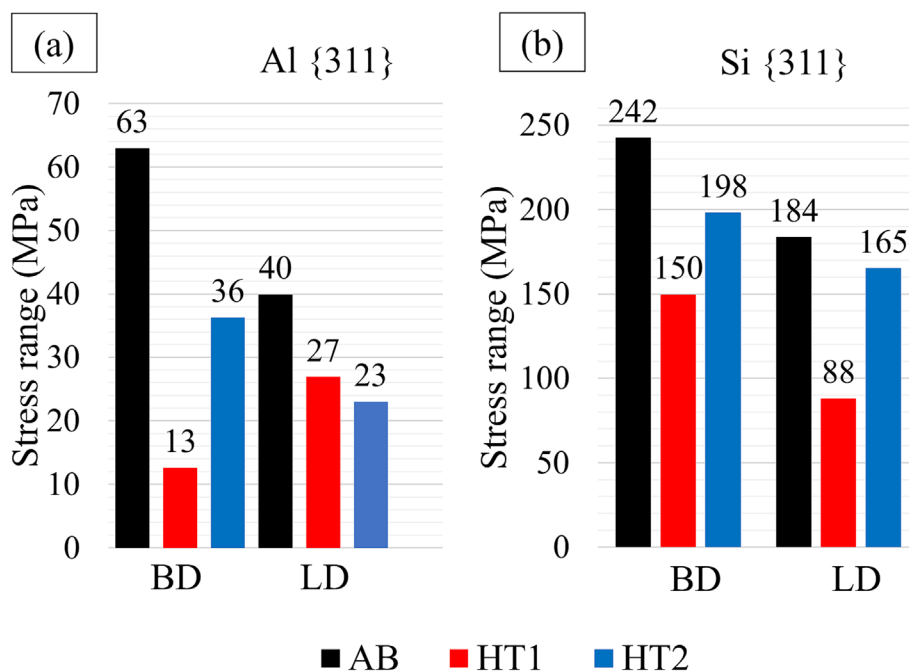


FIGURE 10 Bulk RS ranges before and after heat treatment: difference between maximum and minimum values of the profiles in Figure 7 for (a) the aluminium matrix and (b) the silicon phase.

the volume fraction of the HT1 Si phase to lead to the highest mismatch between the Al and Si phases. Thus, it is assumed that the interconnectivity at the cell walls of the Si network is significantly reduced after HT1. This would lead to a relaxation effect dominating over the expected stressing effect induced by the growing volume percentage of Si phase. Overall and regardless of the mechanisms controlling the Al-matrix to Si-phase mismatch, it is observed that heat treatments disaggregating the Si network (e.g., HT2) do not relieve RS as efficiently as heat treatments preserving such network (e.g., HT1).

It must be noted that the lowest RS state does not necessarily correspond to optimized mechanical performances. In fact, it was reported by these authors that the HT2 static tensile strength is the lowest of the three investigated conditions.¹⁸ Conversely, because of increased ductility, the HT2 material possesses the highest fatigue long crack propagation threshold.¹⁸ Given the small magnitudes of RS present in the investigated samples, it is considered that, in our study, RS play a secondary role in the fatigue crack propagation behaviour of the three investigated conditions. Nevertheless, as shown, for instance, in the case of an as-built PBF-LB/M Ti6Al4V alloy,²⁸ the presence of high magnitude RS clearly influences the crack growth rates and morphology of the crack-path.

4.2 | Lack of trend at the subsurface as observed via EDXRD

The near-surface RS profiles presented in Figure 3 show that, up to a depth of 350 μm , the RS state is not significantly affected by the heat treatment; even though the literature reports relaxation of surface RS induced by the investigated heat treatments.^{29,30} Moreover, the literature also reports that the machining of the surface induces RS of compressive nature.³¹ In other words, the surface finishing, which involves milling and grinding, overrides the differences in surface/sub-surface residual stress induced by the heat treatments. Further assessment of the influence of machining in the RS state is beyond the scope of this work.

4.3 | The effect of porosity on RS measurements: ND versus SXRD

Figure 7c shows that there are two points at about $Y = 10$ mm that do not follow the trend, which is attributed to the presence of porosity clusters. This rationale is based on the significant scatter observed in our previous neutron

diffraction (ND) measurements.¹⁶ Note that a difference of approximately 20 MPa for the matrix RS in both AB and HT1 samples is observed between the data obtained using the SXRD and ND. However, the two experimental campaigns consistently determine the same amount of RS relaxation after heat treatment.

Porosity clusters were identified via micro computed tomography (XCT): the defects are aligned in ~ 0.5 mm wide lines recurring approximately every 1 mm. This porosity is considered the main cause inducing the observed scatter reported in¹⁶ (Figure 11a,b,d,f). A near-rectangular gauge was used in ND experiments (Figure 11b,d), covering an approximate area of 2 mm \times 2 mm in the BD-TD plane. In contrast during SXRD measurements, two different volumes were probed as a function of the investigated component, while a constant gauge length (~ 2.8 mm) was obtained along TD axis (Figure 11c,e,g). Specifically, Figure 11e shows that the amount of porosity probed by the gauge volume corresponding to the BD component (0.225 mm slab) is smaller than that enclosed when measuring the LD component (2 mm slab), or when performing ND (Figure 11d). Therefore, it is considered that the scatter can be reduced when being able to sample an increased number of porosity stripes (clusters) at each measurement point (compare Figure 11f with Figure 11g).

Laboratory EDXRD measurements also display moderate fluctuations in the RS magnitudes (see Figure 8). In this case, the sampling gauge volume resulting from a 1 mm diameter collimator also has the spatial resolution to alternately probe regions where the porosity content is dominant and regions with relatively lower content of porosity. Therefore, the oscillating trend observed in Figure 8 is considered similar in manner to the one observed using ND.¹⁶

In essence, this study proposes a thorough and robust methodology to characterize the RS state over the plane where a fatigue crack will be propagated.¹⁸ The necessity of considering the porosity spatial distribution for conducting

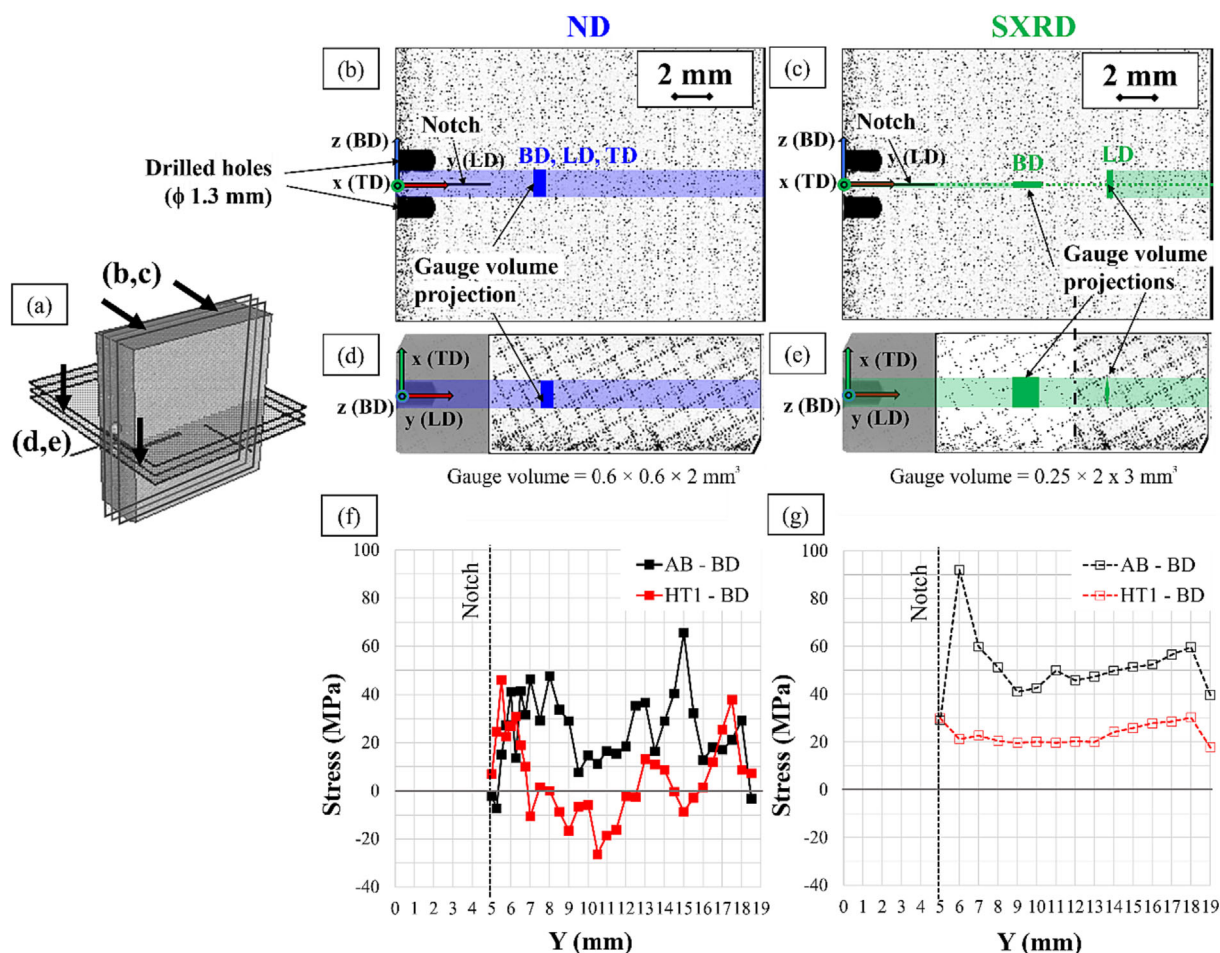


FIGURE 11 (a) 3D rendering and orthographic projections over the TD (b, c) and BD (d, e) axes using a XCT reconstruction of a SENB specimen (pores are represented in black). The porosity content in the volume probed by ND¹⁶ (b, d) and SXRD (c, e) is represented in projection mode. The bands shown in (a) refer to the thickness projected onto the plane. The RS profiles in the notch plane in the AB (black) and HT1 (red) conditions are shown for the corresponding methods used: (f) ND¹⁶ and (g) SXRD.¹⁶

reliable RS determination is emphasized. Care must be taken particularly in the context of AM materials, where such porosity spatial arrangements can greatly differ from case-to-case or even be targeted on demand.

5 | CONCLUSIONS

The effect of two heat treatments (265 °C/1 h and 300 °C/2 h) on the RS state of a PBF-LB/M AlSi10Mg material is investigated. By combining the results obtained from SXRD (bulk) and EDXRD (near surface) techniques, a comprehensive characterization of the RS state on the crack propagation plane of a SENB specimen is performed.

It is found that, because of machining, the RS at the near surface remains constant (and compressive) for all three conditions. The RS in the bulk of the aluminium matrix is predominantly tensile and dependent on the condition. After heat treating at 265 °C for 1 h, the tensile Al matrix stress and the compressive stress in the Si phase decrease in the bulk by up to 60% with respect to the AB condition, whereas a heat treatment at 300 °C for 2 h yields a smaller RS reduction (up to 35% with respect to AB). We thereby conclude that in order to relieve phase specific (micro) RS in such Al-Si alloy, it is important to apply heat treatments that do not fully disaggregate the Si network into discrete particles. It is also observed that HT2 provides the best fatigue crack growth resistance,¹⁸ and thus, the highest RS relief is not necessarily correlated to the best mechanical performance.

ACKNOWLEDGEMENTS

This work is supported by internal Bundesanstalt für Materialforschung und -prüfung (BAM) funding (MIT1-2019-40). The Helmholtz-Zentrum Berlin für Materialien und Energie is acknowledged for granting access to the LIMAX-160 instrument at the X-Ray CoreLab Facility. Camille Pauzon (SIMAP laboratory of Université Grenoble Alpes, Grenoble, France) is acknowledged for her assistance in the Si powder sample preparation. Björn Mieller (Bundesanstalt für Materialforschung und -prüfung, Berlin (BAM), Germany) is also acknowledged for performing the heat treatments. We acknowledge the European Synchrotron Radiation Facility (ESRF) for provision of synchrotron radiation facilities under proposal number MA-5011 and we would like to thank Catherine Dejoie for assistance and support in using the beamline ID22. Open Access funding enabled and organized by Projekt DEAL.

CONFLICT OF INTEREST STATEMENT

The authors declare that they have no known competing financial interests or personal relationships that could have appeared to influence the work reported in this paper.

DATA AVAILABILITY STATEMENT

The data that support the findings of this study are available from the corresponding author upon reasonable request.

ORCID

Itziar Serrano-Munoz  <https://orcid.org/0000-0002-5585-6637>

REFERENCES

- [1] J.-P. Kruth, J. Deckers, E. Yasa, R. Wauthlé, *J Eng Manuf* **2012**, 226, 980. <https://doi.org/10.1177/0954405412437085>
- [2] J. Schröder, A. Evans, T. Mishurova, A. Ulbricht, M. Sprengel, I. Serrano-Munoz, T. Fritsch, A. Kromm, T. Kannengießer, G. Bruno, *Metals* **2021**, 11, 1830. <https://doi.org/10.3390/met11111830>
- [3] Z. Jiang, J. Sun, F. Berto, X. Wang, G. Qian, *Phys Mesomech* **2023**, 26(4), 367. <https://doi.org/10.1134/S102995992304001X>
- [4] J. Fiocchi, A. Tuissi, P. Bassani, C. A. Biffi, *J Alloys Compd* **2017**, 695, 3402. <https://doi.org/10.1016/j.jallcom.2016.12.019>
- [5] X. X. Zhang, A. Lutz, H. Andrä, M. Lahres, W. M. Gan, E. Maawad, C. Emmelmann, *Int J Plast* **2021**, 139, 102946. <https://doi.org/10.1016/j.ijplas.2021.102946>
- [6] P. Van Cauwenbergh, V. Samaee, L. Thijs, J. Nejezhlebova, P. Sedlak, A. Ivekovic, D. Schryvers, B. Van Hooreweder, K. Vanmeensel, *Sci Rep* **2021**, 11(1), 6423. <https://doi.org/10.1038/s41598-021-85047-2>
- [7] F. Lasagni, B. Mingler, M. Dumont, H. P. Degischer, *Mater Sci Eng A* **2008**, 480(1-2), 383. <https://doi.org/10.1016/j.msea.2007.07.008>
- [8] B. J. Mfusi, N. R. Mathe, L. C. Tshabalala, P. A. Popoola, *Metals* **2019**, 9(11), 1216. <https://doi.org/10.3390/met9111216>
- [9] L. Tonelli, E. Liverani, A. Morri, L. Ceschini, *Metall Mater Trans B* **2021**, 52, 2484. <https://doi.org/10.1007/s11663-021-02179-6>
- [10] J. Fiocchi, A. Tuissi, C. A. Biffi, *Mater Des* **2021**, 204, 109651. <https://doi.org/10.1016/j.matdes.2021.109651>
- [11] M. Bonneric, C. Brugger, B. Tranchand, A. C. Moreno, J. Lesseur, N. Saintier, *Int J Fatigue* **2024**, 181, 108154. <https://doi.org/10.1016/j.ijfatigue.2024.108154>

- [12] I. Serrano-Munoz, I. Roveda, A. Kupsch, B. R. Müller, G. Bruno, *Mater Sci Eng A* **2022**, 838, 142732. <https://doi.org/10.1016/j.msea.2022.142732>
- [13] L. Zhao, J. G. Santos Macías, L. Ding, H. Idrissi, A. Simar, *Mater Sci Eng A* **2019**, 764, 138210. <https://doi.org/10.1016/j.msea.2019.138210>
- [14] C. Colombo, C. A. Biffi, J. Flocchi, A. Tuissi, *Key Eng Mater* **2019**, 813, 364. <https://doi.org/10.4028/www.scientific.net/KEM.813.364>
- [15] P. Van Cauwenbergh, A. Beckers, L. Thijs, B. Van Hooreweder, K. Vanmeensel, Heat Treatment Optimization via Thermo-Physical Characterization of AlSi7Mg and AlSi10Mg Manufactured by Laser Powder Bed Fusion (LPBF), Euro PM2018 Congress, Euro PM2018 Congress Proceedings, **2018**.
- [16] I. Roveda, I. Serrano-Munoz, T. Mishurova, M. Madia, T. Pirling, A. Evans, M. Klaus, J. Haubrich, G. Requena, G. Bruno, *J Mater Sci* **2022**, 57(48), 22082. <https://doi.org/10.1007/s10853-022-07997-w>
- [17] I. Roveda, *Investigation of Residual Stress and Microstructure Effects on the Fatigue Behaviour of an Aluminium-Silicon Eutectic Alloy Produced by Laser Powder Bed Fusion*, Technische Universität Darmstadt, Darmstadt **2023**.
- [18] I. Roveda, I. Serrano-Munoz, J. Haubrich, G. Requena, M. Madia, *Int J Fatigue* **2023**, 175, 107808. <https://doi.org/10.1016/j.ijfatigue.2023.107808>
- [19] N. Takata, M. Liu, H. Kodaira, A. Suzuki, M. Kobashi, *Addit Manuf* **2020**, 33, 101152. <https://doi.org/10.1016/j.addma.2020.101152>
- [20] ID22 - High resolution powder diffraction beamline, **2023**. <https://www.esrf.fr/id22>
- [21] I. Serrano-Munoz, A. Evans, I. Roveda, T. Mishurova, MA-5011: Evaluation of inter-phase strains present in as-built and heat treated LPBF AlSi10Mg materials, In: <https://doi.esrf.fr/10.15151/ESRF-ES-819996597> (Ed.) **2022**.
- [22] A. Fitch, C. Dejoie, E. Covacci, G. Confalonieri, O. Grendal, L. Claustre, P. Guillou, J. Kieffer, W. de Nolf, S. Petitdemange, M. Ruat, Y. Watier, *J Synchrotron Radiat* **2023**, 30(5), 1003. <https://doi.org/10.1107/S1600577523004915>
- [23] ISO-21432. Non-Destructive Testing—Standard Test Method for Determining Residual Stresses by Neutron Diffraction. **2019**.
- [24] F. Bayerlein, F. Bodensteiner, C. Zeller, M. Hofmann, M. F. Zaeh, *Addit Manuf* **2018**, 24, 587. <https://doi.org/10.1016/j.addma.2018.10.024>
- [25] L. M. Sochalski-Kolbus, E. A. Payzant, P. A. Cornwell, T. R. Watkins, S. S. Babu, R. R. Dehoff, M. Lorenz, O. Ovchinnikova, C. Duty, *Metal Mater Trans A* **2015**, 46(3), 1419. <https://doi.org/10.1007/s11661-014-2722-2>
- [26] A. Ulbricht, S. J. Altenburg, M. Sprengel, K. Sommer, G. Mohr, T. Fritsch, T. Mishurova, I. Serrano-Munoz, A. Evans, M. Hofmann, G. Bruno, *Metals* **2020**, 10(9), 1234. <https://doi.org/10.3390/met10091234>
- [27] X-ray CoreLab at Helmholtz-Zentrum Berlin für Materialien und Energie. <https://www.optik-bb.de/news/artikel/x-ray-corelab-steht-bereit/>
- [28] B. Vrancken, V. Cain, R. Knutsen, J. Van Humbeeck, *Scr Mater* **2014**, 87, 29. <https://doi.org/10.1016/j.scriptamat.2014.05.016>
- [29] S. Marola, S. Bosia, A. Veltro, G. Fiore, D. Manfredi, M. Lombardi, G. Amato, M. Baricco, L. Battezzati, *Mater Des* **2021**, 202, 109550. <https://doi.org/10.1016/j.matdes.2021.109550>
- [30] Y. Chen, H. Sun, Z. Li, Y. Wu, Y. Xiao, Z. Chen, S. Zhong, H. Wang, *Materials (Basel)* **2020**, 13(2), 451. <https://doi.org/10.3390/ma13020451>
- [31] S. Beretta, L. Patriarca, M. Gargourimotlagh, A. Hardaker, D. Brackett, M. Salimian, J. Gumpinger, T. Ghidini, *Mater Des* **2022**, 218, 110713. <https://doi.org/10.1016/j.matdes.2022.110713>

SUPPORTING INFORMATION

Additional supporting information can be found online in the Supporting Information section at the end of this article.

How to cite this article: I. Roveda, T. Mishurova, A. Evans, A. N. Fitch, J. Haubrich, G. Requena, G. Bruno, I. Serrano-Munoz, *Strain* **2024**, e12475. <https://doi.org/10.1111/str.12475>